Heliyon 6 (2020) e03987

Contents lists available at ScienceDirect

Heliyon

journal homepage: www.cell.com/heliyon

Research article

Simulation and validation of residual deformations in additive manufacturing of metal parts

Thomas Mayer *, Gabriel Brändle, Andreas Schönenberger, Robert Eberlein

Institute of Mechanical Systems, Zurich University of Applied Sciences, Winterthur, Switzerland

ARTICLE INFO

Keywords:
Industrial engineering
Manufacturing engineering
Computational mechanics
Process modeling
Computer-aided engineering
Solid mechanics
Welding
Mechanical property
Structural analysis
Structural behavior
Additive manufacturing
Selective laser melting
Process simulation
Distortion
Shape deviation
Inherent strain method
Thermo-mechanical simulation
Calibration
Validation
ANSYS

ABSTRACT

Selective laser melting (SLM) is gaining increasing relevance in industry. Residual deformations and internal stresses caused by the repeated layerwise melting of the metal powder and transient cooling of the solidified layers still presents a significant challenge to the profitability and quality of the process. Excessive distortions or cracking may lead to expensive rejects. In practice, critical additively manufactured parts are either iteratively pre-compensated or redesigned based on production experience. To satisfy the need for improved understanding of this complex manufacturing process, CAE software providers have recently developed solutions to simulate the SLM process. This study focuses on the evaluation of two solutions by ANSYS, i.e. ANSYS Additive Print and ANSYS Additive Suite.

ANSYS Additive Print (AAP), a user-oriented software, and ANSYS Additive Suite (AAS), a software requiring advanced experience with Finite Element Methods (FEM), are investigated and validated with regard to residual deformations. For the evaluation of the two programs, calibration and validation geometries were printed by SLM in Ti–6Al–4V and residual deformations have been measured by 3D scanning. The results have been used for the calibration of isotropic and anisotropic strain scaling factors in AAP, and for sensitivity analyses on the effect of basic model parameters in AAS. The actual validation of the programs is performed on the basis of different sample geometries with varying wall thickness and deformation characteristic.

While both simulation approaches, AAP and AAS, are capable of predicting the qualitative characteristics of the residual deformations sufficiently well, accurate quantitative results are difficult to obtain. AAP is more accessible and yields accurate results within the calibrated regime. Extrapolation to other geometries introduces uncertainties, however. AAS, on the other hand, features a sounder physical basis and therefore allows for a more robust extrapolation. Numerical efforts and modelling uncertainties as well as requirements for an extensive set of material parameters reduce its practicality, however. More appropriate calibration geometries, continuing extension of a more reliable material database, improved user guidelines and increased numerical efficiency are key in the future establishment of the process simulation approaches in the industrial practice.

1. Introduction

Selective Laser Melting (SLM) is an Additive Manufacturing (AM) process in which a metal powder alloy is melted layer by layer by a laser beam. In each layer, the laser scans over each cross-section of the printed part while continuously focusing energy to spots in the micrometer range. Due to the local heat input, the component does not cool homogeneously so that severe thermal gradients are introduced [1, 2]. These typically lead to thermal strains in the volume surrounding the melt pool [3]. As these thermal strains accumulate during transient melting and solidification in the layerwise SLM process, they cause residual deformations (distortions) and stresses in the final AM part. Excessive distortion and cracking can thereby lead to expensive rejects in the AM process when respective quality criteria cannot be met. Obviously, this imposes significant economic challenges during the application of e.g. SLM in the industrial practice [4].

The extent of residual macroscopic distortions is a result of three factors: 1) the local *melt pool geometry*, 2) the *scan strategy*, and 3) the actual *part geometry*, [5, 6, 7, 8, 9, 10, 11, 12].

Significant effort has been put into the characterization and physical understanding of the *melt pool geometry* resulting from different process parameter sets. This is mainly determined by complex multi-physical and

* Corresponding author.
E-mail address: mayt@zhaw.ch (T. Mayer).

https://doi.org/10.1016/j.heliyon.2020.e03987
Received 23 December 2019; Received in revised form 30 March 2020; Accepted 12 May 2020

highly non-linear interactions between the laser beam (power, speed), the metal powder (material, particle size and its distribution, layer thickness) and the resulting melt volume, e.g. [13]. Together with the *scan strategy* (laser speed, path/pattern, hatch spacing) [14], the process parameters and therefore the melt pool geometry has a decisive effect on the resulting local microstructure (e.g. pore volume, grain size). Several aspects of these multi-physical phenomena have been studied both experimentally and by detailed multi-physics simulation, e.g. [15, 16]. Such simulations are, however, sophisticated, numerically expensive and difficult to validate effectively. In this respect, these methods are mainly justified to gain physical understanding of the local SLM process but they are inefficient to predict macroscopic distortions or residual stress induced cracking. A review and classification of different modelling approaches in the context of additive manufacturing is given in [17].

While melt pool geometry together with the scan strategy mainly affect the local microstructure in the AM part, the actual part geometry plays a significant role for the build-up of macroscopic residual distortions or stresses. The local heat input of the laser dissipates through the already solidified component and support structures to the build plate as well as to the surrounding powder and gas environment by conduction, convection and radiation, e.g. [18]. Thermal strains are a result of temperature gradients. As the cool down path is mainly determined by the part and support geometries as well as the build orientation, these play a decisive role in the build-up of residual distortions and stresses. Besides these geometrical aspects, the scan strategy (laser speed, path/pattern, hatch spacing and stripe width), not only determines the quality of the microstructure but also the anisotropy of the resulting distortion, e.g. [19]. Different Finite Element (FE) based simulation approaches have been developed that allow to predict the residual distortion and stresses of parts that are manufactured by powder-bed methods such as SLM. These range from numerically more expensive approaches simulating the weakly and strongly coupled thermal and mechanical histories during the melting, cool-down and solidification of material volumes along the laser pat, e.g. [20], to simplified inherent strain methods, e.g. [21, 22], in which complete material layers are activated with a given directional strain (i.e. inherent strain) that can be calibrated to actual material data, e.g. [23, 24].

In practice, AM designs are often adapted based on experience by either pre-compensating the expected deformation or by optimizing the support and/or scan strategy to avoid expensive rejects due to residual distortions or cracking. Due to the complex nature of the SLM process, this is an iterative, time and cost intensive procedure that essentially relies on the experience of the machine operators. CAE software providers have recently introduced commercial FE solutions with the goal to simulate residual distortions and stresses before expensive production trials need to be made in order to move away from experience based AM design to a simulation based design method. Thereby, manufacturing information can be propagated backwards into the design phase to best shape an additively manufactured component and to take best advantage of this advanced manufacturing technology [25]. To date, various software solutions are available in different stages of their development. These include e.g. Additive Works by Amphyon, Additive Print and Suite by ANSYS, Netfabb by Autodesk, Simufact by MSC, Simcenter 3D Additive Manufacturing by Siemens, and 3DS Experience by Dassault Systems. Industrial applications of these tools have been recently presented e.g. in [26, 27, 28, 29].

This study focuses on the evaluation of two solutions by ANSYS, i.e. ANSYS Additive Print and ANSYS Additive Suite. First, ANSYS Additive Print has been fully calibrated to Ti–6Al–4V parts that were additively manufactured by SLM on an EOS M290 machine. Furthermore, sensitivity studies are presented assessing the influence of mesh size and type as well as material input parameter variations in ANSYS Additive Suite. Finally, both tools are validated by comparing their residual deformation predictions for other sample geometries featuring different wall thicknesses and shapes with 3D measurements of actually printed parts. The goal of this study is to provide a reality check of an advanced commercial software tool and to point out practical issues that arose during this work as a guideline for potential users.

2. Methods

The Finite Element (FE) simulation software packages ANSYS Additive Print (AAP) and ANSYS Additive Suite (AAS) are intended to simulate the SLM process to avoid unplanned machine downtime and improve part quality. By predicting deformations and stresses in AM parts during the manufacturing process, these tools form the basis for assessing their design integrity. Residual deformations of AM components can be predicted and compensated prior to starting the actual manufacturing process. Both simulation options use a layered discretization with voxel elements (i.e. cubic hexahedral finite elements with defined edge length), e.g. [30, 31, 32]. For AAP, a voxel size of at least a fourth of the minimum feature size (minimum wall thickness) is recommended but limited to a range of 0.02–2 mm. Besides Cartesian voxel (HEX) elements, AAS offers layered tetrahedral (L-TET) elements for better shape adaptation. For both element types, a layer height of 10–20 times the actual metal powder layer thickness is recommended for the built part as an appropriate balance between accuracy and numerical effort. The element size for the base plate is chosen to be 10 times larger than the element size of the built body.

For this study ANSYS version 2019R1 was used. Different modelling approaches are followed by the two software solutions AAP and AAS as described in the following.

2.1. Simulation approach

2.1.1. ANSYS Additive Print (AAP)

AAP is a user-oriented software for simplified simulation of SLM processes, based on a limited number of material input parameters: elastic modulus and Poisson ratio as well as yield strength and bilinear elastic-plastic deformation characteristics are required [33], cf. Table 1.

Within AAP, the SLM build-up process is simulated by layerwise activation of voxel elements that initially all feature the same inherent strain. After activation of every voxel layer, the deformation at mechanical equilibrium is calculated. The applied initial inherent strain is a priori assumed to be equal to the strain at the yield stress, i.e. σ_y/E, and needs to be calibrated to actually printed calibration geometries [34]. The calibration thereby inherently includes information on the machine specific AM process and the material specific response.

The software offers both purely elastic or elastic-plastic simulation options for the following three simulation types. In this study, the J2 plasticity model has been used to more accurately predict the residual stress level and the associated residual deformation.

2.1.1.1. Assumed Strain (AS). This is the simplest and fastest simulation type within AAP assuming a predefined isotropic inherent strain in each voxel element. Anisotropic effects or process dependencies are not directly considered and AS relies solely on material and machine specific calibrations of the isotropic Strain Scaling Factor (*SSF*). This is an isotropic scaling factor for the predicted inherent strain ε_{inh}, cf. Eq. (1), to better match simulation and measurements.

$$\varepsilon_{inh} = SSF \cdot \frac{\sigma_y}{E} \tag{1}$$

AS does further not consider thermal cycling effects which may be important in cases where a printed layer does not cool down homogeneously e.g. due to geometrical features like holes. Neither process nor scan strategy parameters are required for this simulation type.

2.1.1.2. Scan pattern (SP). The SP approach takes the scanning direction into account. Larger distortions occur along the laser scanning direction than perpendicular to it. Thereby, a significant anisotropic distortion is

Table 1. Ti–6Al–4V material input data for AAP.

Stress Mode	J2 plasticity
Hardening Factor	0.0198 [-]
Yield Strength	1′100 MPa
Elastic Modulus	110′000 MPa
Poisson Ratio	0.3 [-]

introduced. This behavior is considered by appropriately calibrating the Anisotropic Strain Coefficients (*ASC*) in addition to the isotropic *SSF*. In contrast to the SSF, ASCs scale the applied anisotropic inherent strain separately for the longitudinal ($ASC_{\parallel}$) and transverse ($ASC_{\perp}$) scan directions as well as the build direction (ASC_z). Like this, the inherent strain components $\varepsilon_{inh,\parallel}$, $\varepsilon_{inh,\perp}$ and $\varepsilon_{inh,z}$ in longitudinal, transverse scan and in build direction, respectively, are calculated by Eq. (2).

$$\varepsilon_{inh,\parallel} = ASC_{\parallel} \cdot SSF \cdot \frac{\sigma_y}{E} \quad \varepsilon_{inh,\perp} = ASC_{\perp} \cdot SSF \cdot \frac{\sigma_y}{E} \quad \varepsilon_{inh,z} = ASC_z \cdot SSF \cdot \frac{\sigma_y}{E} \tag{2}$$

In addition to the standard parameters defined for AS, scan strategy parameters like start and rotation angles of the scan direction need to be specified. Simulations in SP take slightly longer with the same voxel size and the same material behavior than in AS.

2.1.1.3. Thermal strain (TS). The TS simulation type constitutes the most accurate approach within AAP as thermal ratcheting effects (i.e. accumulation of thermal strain due to local re-heating of already solidified layers) and inhomogeneous cooling are considered. As TS requires a thermal simulation prior to the mechanical solution, this approach is numerically significantly more expensive. Analogous to the SP approach, both isotropic and anisotropic strain scaling coefficients need to be calibrated on the basis of measured data. In addition to the material and scan strategy parameters, TS also requires actual process and scan strategy parameters like laser power and speed, baseplate temperature and layer thickness as well as hatch spacing and stripe width, see Table 2.

All three simulation approaches in AAP require machine and material specific calibration to a predefined calibration geometry. ANSYS specifies a Cross Wall geometry with a wall thickness of 10 mm (CW10, cf. Figure 1) for this purpose which needs to be printed with a bidirectional scan strategy [34, 35]. This specification does, however, neither consider a separate contour strategy to improve the surface quality of AM parts nor manufacturing of multiple parts on one build plate as it is common practice. Negligence of the contour strategy during the calibration process can lead to significant deviations for thin-walled parts where the surface-to-volume ratio is larger and the surface constitutes a substantial share of the part. A non-negligible dwell time further lies between every layer of each part. This consists of the recoating time as well as the laser exposure period spent for other parts on the same build plate. Thereby, the effective cool-down time between every layer of each part and the resulting residual distortions are strongly affected. Typically, the part quality and thereby also the distortion may vary with the location of the parts on the build plate as the thermal boundary conditions vary with the local gas flow conditions [36, 37] and the mechanical properties are affected by the recoating direction [38].

In order to take account of these effects, calibration of the AAP simulation types was performed on two CW10 samples that were printed together with other validation geometries on the same build plate. Thereby, bidirectional scan strategies are applied for the volume and a conventional contour strategy for the surface sections. For each of the two calibration samples, the bidirectional scan strategy was rotated by 90° with respect to the recoating and gas flow direction in order to take potential effects into account. While a voxel size of 0.25 mm is specified for the calibration process, a pre-calibration was performed with 0.4 mm voxels to obtain a first calibration parameter set quickly. This was then used as a starting point for the final optimization iterations with 0.25 mm.

Table 2. Process parameter input data for AAP.

Laser Power	340 W
Scan Speed	1250 mm/s
Layer Thickness	60 µm
Baseplate Temperature	35 °C
Hatch Spacing	75 µm
Slicing Stripe Width	5 mm

2.1.2. ANSYS Additive Suite (AAS)

In contrast to AAP as a stand-alone software tool, AAS is fully embedded in the ANSYS Workbench environment. It is a weak thermo-mechanically coupled simulation, i.e. a thermal calculation is performed prior to the mechanical simulation for which the transient temperature history acts as an input variable. The built part is first meshed as a whole by either layered voxel (HEX) or tetrahedral (L-TET) elements. Each finite element layer (super layer) represents a number of actual metal powder layers assuming that the thermal histories of neighboring physical layers are comparable and can be lumped into one representative layer. For the actual process simulation, each super layer is activated sequentially using a standard element birth and death technique. The respective thermal boundary conditions are thereby evolving with the generated part. The thermal boundary condition between the solidified part and the surrounding powder is simplified by an equivalent convective heat transfer condition to avoid modelling of the powder material itself. Each super layer is activated as a whole at the melting temperature of the material and cooling down during a process parameter dependent time period until the next super layer is activated (i.e. dwell time). The dwell time defines how long the powder deposition of a layer and the cooling process between the layers takes. During the cool-down period, thermal strains occur according to the local temperature gradient and the respective thermal expansion coefficient. For more efficient computation times, the temporal discretization is chosen to be rather coarse assuming that the fast thermal transients are not influencing the thermal and plastic strains resulting during the cool down period. The moving heat source (i.e. laser scan pattern) is not accounted for, assuming that the thermal gradient in the build direction dominates over the in-plane thermal gradient with respect to its influence on the residual deformations.

Due to the consideration of the temperature field and the actual local thermal strains of the solidified material, AAS is more realistic than AAP. This comes, however, at an increased numerical cost. Major assumptions are made when the laser scan pattern is neglected. In AAS significantly more input parameters are required compared to AAP. Basic temperature dependent material properties need to be specified for process simulations and no additional calibration is required. These include elastic modulus, Poisson ratio and elastic-bilinear plastic stress-strain curves as well as density, coefficient of thermal expansion, orthotropic thermal conductivity and specific heat-capacity up to the melting temperature of the material. For this study, the material properties for Ti–6Al–4V (AM material version) as predefined by ANSYS was used. Furthermore, the process parameters as defined in Table 2 were used for simulations with AAS. In addition, the inert gas temperature is assumed as 22 °C and the powder temperature during the build process as 35 °C. Gas and powder convection coefficients of $1 \cdot 10^{-5}$ W/mm^2·°C at a powder property factor of 0.01 were further applied. As the build job included multiple test geometries (see Section 2.2), an increased dwell time of 69.5 s was applied as calculated from the average cross-sectional area and the laser scan parameters. Besides the built part geometry, the base plate also needs to be included in the model. While the voxel and layered-tetrahedral element sizes were varied for the built part, the base plate was only meshed with a hexahedral element size of 10 mm. As AAP only calculates residual deformations for an infinitely stiff base plate, all

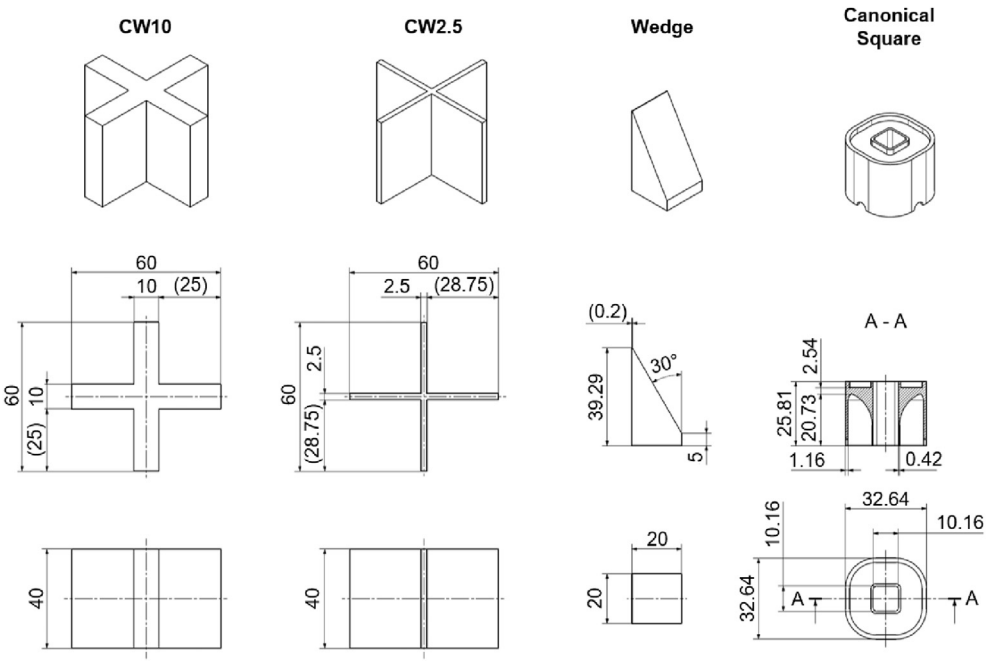

Figure 1. Calibration (CW10) and validation (CW2.5, Wedge and Canonical Square) geometries.

simulations in this study have been evaluated for test geometries still attached to the fixed base plate for better comparability.

2.2. Test geometries and additive manufacturing

Various test geometries have been manufactured by SLM for calibration and validation purposes. Figure 1 gives an overview and relevant dimensions of the four different sample types investigated in this study.

2.2.1. Cross Wall (CW10)

The Cross Wall geometry with a wall thickness of 10 mm corresponds to the standard calibration geometry for AAP [34, 35]. Bidirectional printing of the structure yields information for the determination of the anisotropic strain scaling factors (*ASC*) as one leg is printed with the scan direction along its longitudinal direction and the other leg transverse to the longitudinal direction. The former is expected to feature larger residual distortions than the latter due to the thermal gradients induced by the melt pool. Additional information on the isotropic strain scaling factor (*SSF*) comes from the 67° rotating scan direction. For this sample a contour scan has been used. The surface to volume ratio of 0.268 mm is relatively small, however, so that the difference between volume and surface scan strategies is expected to be negligible.

2.2.2. Cross Wall (CW2.5)

A Cross Wall geometry with a wall thickness of 2.5 mm was additionally studied to validate the extrapolation quality of AAP to different wall thicknesses as calibrated. In contrast to the CW10 sample, the surface to volume ratio of 0.867 mm is significantly higher so that a more significant influence of the contour strategy on the global residual distortion is expected.

2.2.3. Wedge

For further validation of the robustness of AAP towards continuous wall thickness changes, a Wedge sample was further printed. The wall thickness changes from 20 to 0.2 mm in a 30° angle. With only 20% of the volume of CW10 the goal was further to check whether this sample would be a more economical alternative to the bulkier CW10 calibration sample. For this reason, the Wedge sample was also printed with two bidirectional and a rotating scan strategy.

2.2.4. Canonical Square

A more complex geometry is further investigated with the Canonical Square sample as developed during the America Makes Project #4026 [39]. This sample geometry features two different wall thicknesses for the inner (0.42 mm) and outer (1.16 mm) tubes that are both significantly smaller than the CW10 calibration sample. The Canonical Square was only printed using a 67° rotating scan strategy. Due to a deformation mechanism that is dominated by z- rather than x/y- thermal strains, this constitutes a validation case for more complex geometries.

The outline of the calibration and validation samples on the build plate with the respective scan strategies is shown in Figure 2. CW10, CW2.5 and the Wedge samples are printed with two different bidirectional and a 67° rotating scan strategy. The two bidirectional scan strategies are equivalent but rotated by 90° with respect to the global build plate reference system. The Canonical Square sample is only printed with a 67° rotating scan strategy. In order to identify the orientation of the build plate and as a reference for the 3D measurement of the printed samples, two rectangular reference bodies have been printed.

All test geometries have been printed on an EOS M290 SLM machine in an inert argon atmosphere using Ti–6Al–4V powder by EOS with an average particle size of 50.6 µm. Standard process parameters as indicated in Table 2 with contour scans have been applied for the manufacturing of the samples. Thereby, all test geometries have been printed without support structures directly onto the base plate (Ti–6Al–4V, 250 × 250 × 25 mm). The total build volume amounts to approximately 250′000 mm^3.

2.3. 3D measurements

For the quantitative characterization of the residual distortions after printing 3D laser scanning was applied. The actual printed test geometries were measured while still being attached to the plate by means of a 3D Laser Creaform HandyScan3D 700 with a volumetric accuracy of ±50 µm under the given conditions. During measurement, special care was taken to ensure that the sides of the cross walls are acquired with high resolution as they are needed for validation.

The recorded data was first analyzed and cleaned with the software VXelements. Further adjustments to the resulting STL file and the separation of the individual parts was performed in the CAD program CATIA

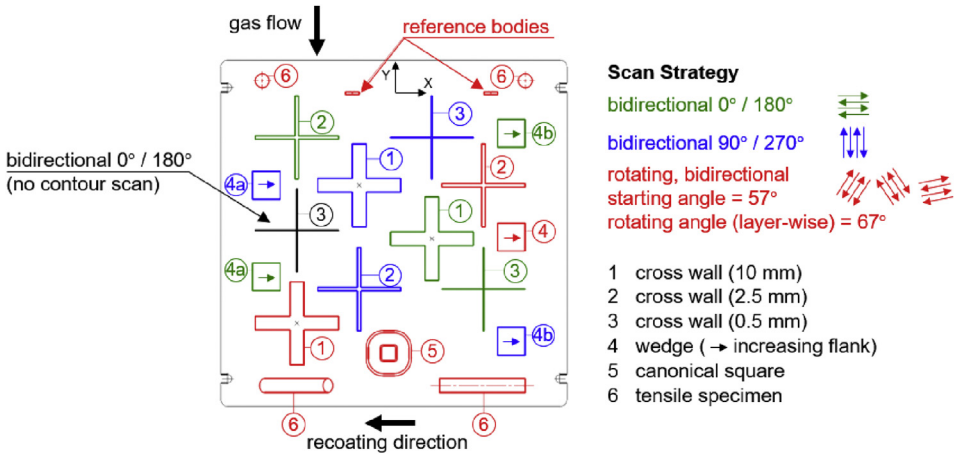

Figure 2. Outline of build plate for calibration and validation parts with different scan strategies.

V5. To determine the shape deviation of the printed parts, the measured 3D geometry is fitted to the target structure, cf. Figure 3. The shape deviations d_{x^+}, d_{x^-}, d_{y^+} and d_{y^-} in positive and negative x- and y-directions, respectively, can then be evaluated. A direct evaluation of the shape deviation depends, however, on the underlying fit of the measured to the target geometry. This is considerably influenced by the initial conditions for the geometrical fit. Alternatively, the width deviations $\Delta x = \overline{W}_x - W_x$ and $\Delta y = \overline{W}_y - W_y$ and in x- and y-directions, respectively, can be evaluated from the measured ($\overline{W}_x$, $\overline{W}_y$) and targeted (W_x, W_y) widths in the x- and y-directions.

Figure 4 compares the empirical standard deviations for these two evaluation variants along the central vertical paths of the sample sides when the measured geometry is fitted with different four initial positions. The standard deviation is around 0.015 mm for the simple shape deviation while an evaluation on the basis of the width deviation is smaller than 0.005 mm away from the edges of the sample. For this reason the width deviation is chosen as an appropriate evaluation parameter. Further scatter of the width deviation in the order of ±50 µm is expected from the surface roughness of the printed parts where eventually metal powder particles can remain after the SLM process [40].

3. Results and discussion

3.1. Residual deformations

Evaluation of the width deviations over the sample heights from the 3D laser scans of the printed calibration (CW10) and validation samples (CW2.5, Wedge, Canonical Square) are shown in Figures 5, 6, 7, and 8. Measurement values at the sample edges are neglected due to significant edge effects of the 3D scanning method.

Width deviations in CW10 are relatively insensitive to scan strategy and position of the samples, cf. Figure 5. The characteristics show a slight asymmetry of the width deviation over the sample height which could be attributed to a higher stiffness closer to the bulk build plate that constrains excessive thermal expansion in the first layers. Maximum width deviations are in the range of 0.5–0.6 mm. Noticeable are the pronounced differences of up to 0.1 mm for the width deviations in the y-direction of the 0°/180° bidirectional printed geometry (green dashed) at the height range of $z = 5$–20 mm, and of the rotating printed geometry (red dashed) between $z = 23$ mm and 39 mm. Meanwhile, the width deviations in the x-directions are largely comparable. This indicates a significant effect of the sample position and orientation with respect to the incoming inert gas flow that leads to variations of the thermal boundary conditions for the printed parts. It is further striking that the 67° rotating sample features much more pronounced fluctuations in the range of up to 50 µm than the other samples. This is attributed to a higher surface roughness due to the presence of powder particles on the surface, cf [41].

A similar distortion characteristic is found for the CW2.5 samples, cf. Figure 6. Due to the reduced stiffness of the thinner parts, the maximum width deviation is 0.05–0.1 mm higher than for the CW10 samples. A more pronounced effect of the sample position is further observed for the CW2.5 samples. Width deviations for the 0°/180° (green dashed) and 90°/270° (blue solid) bidirectional samples should be comparable in the x- and y-directions, respectively. They differ, however, by approximately 0.05 mm over a large portion of the height. Again, this is attributed to the inert gas flow as the 0°/180° bidirectional sample (green) is exposed more directly to the gas flow than the 90°/270° sample that is surrounded by several other samples. A significant anisotropy of 0.05–0.2 mm is further observed for the 0°/180° bidirectional (green) sample for heights up to 10 mm. The 67° rotating samples (red) largely fall in line with the 90°/270° bidirectional sample while small differences between

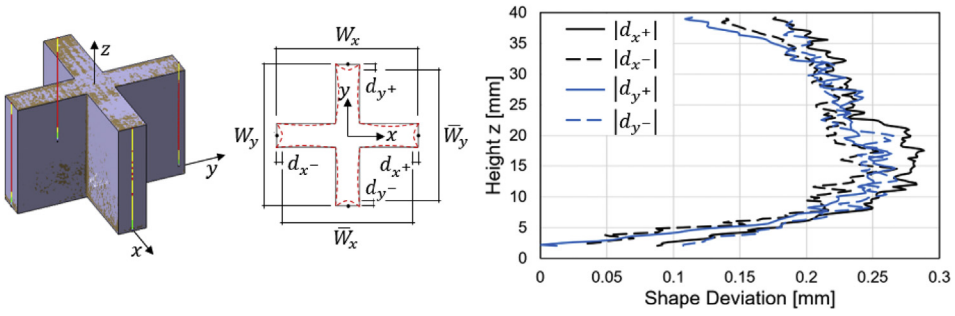

Figure 3. Directional shape deviations in positive and negative x- and y-directions, respectively, as measured from the sample center as determined by least-squares fits of actual and target geometries (CW10).

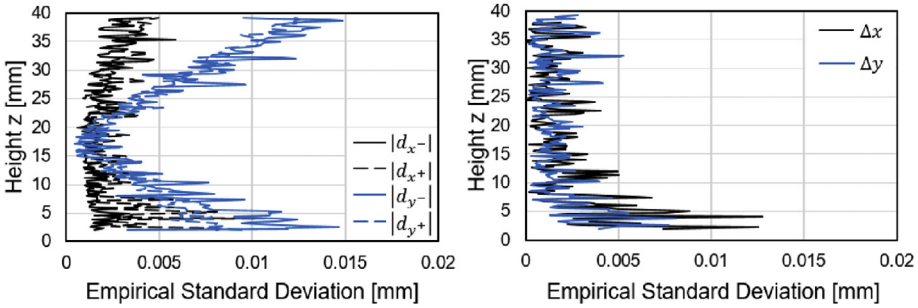

Figure 4. Comparison of empirical standard deviations from four repeated measurements when measuring directional shape deviations ($d_{x^-}, d_{x^+}, d_{y^-}, d_{y^+}$) and width deviations ($\Delta x, \Delta y$).

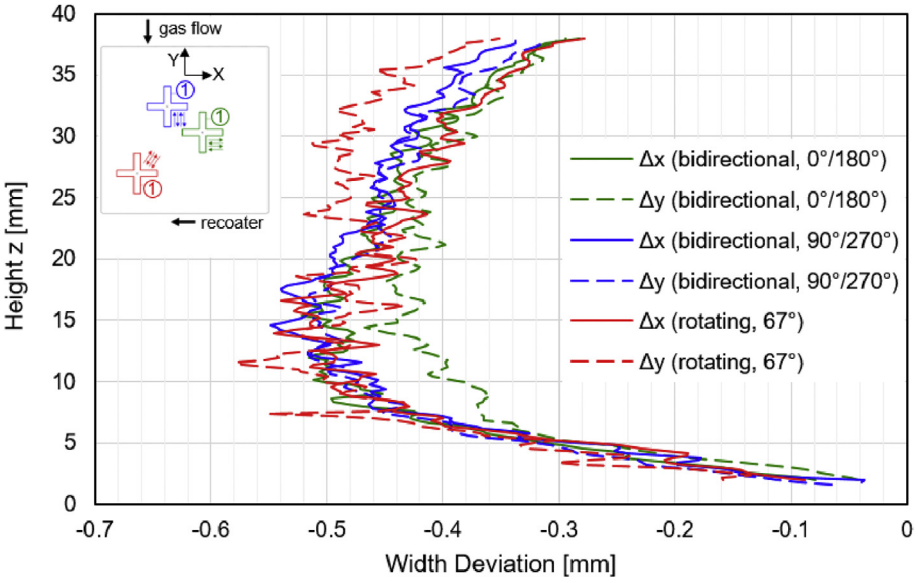

Figure 5. CW10: Measured width deviations in *x*- and *y*-directions for bidirectional and rotating scan strategies.

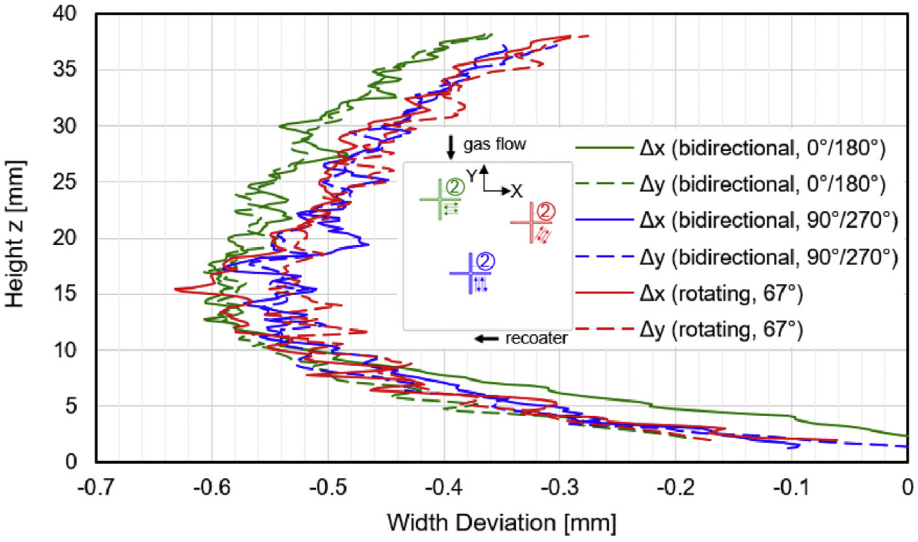

Figure 6. CW2.5: Measured width deviations in *x*- and *y*-directions for bidirectional and rotating scan strategies.

the width deviations in *x*- and *y*-direction occur at a height of $z = 15$mm. The effect of the wall thickness on the shape deviations is negligible, however, when compared to the bidirectionally printed samples. Also for CW2.5 fluctuations of the width change in the order of 50 µm are observed that are attributed to the surface roughness and powder particles on the surface.

In contrast to the Cross Wall samples, the width deviations of the Wedge geometry appear to be only half, cf. Figure 7. The width deviation

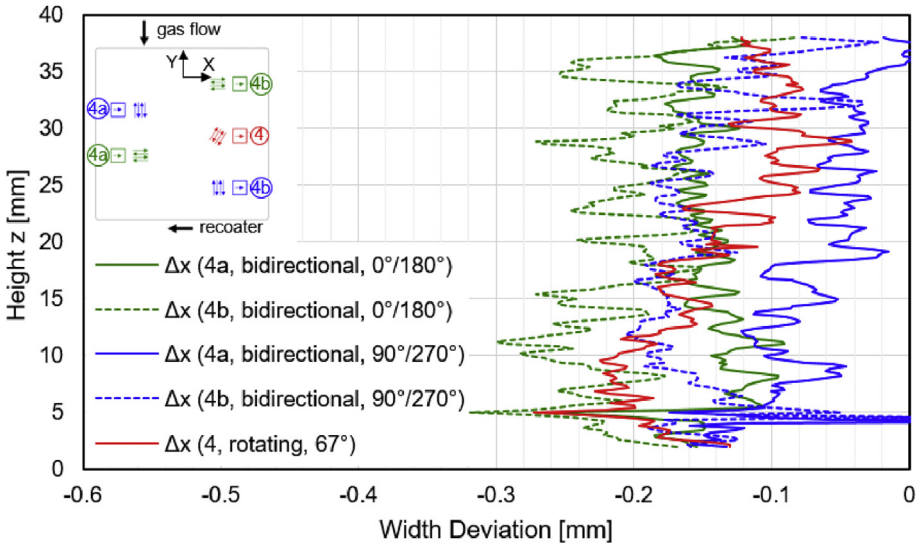

Figure 7. Wedge: Measured width deviations in *x*- and *y*-directions for bidirectional and rotating scan strategies.

is measured as the change in width in the *x*-direction between the oblique flank and the straight back wall. Furthermore, the scatter of the width deviation is rather large and in the range of more than ±50 µm. This is attributed to the high surface roughness in the oblique part as compared to the straight edges of the Cross Wall samples. The effect of the sample position (solid to dashed lines) is in the order of 0.1 mm and therewith in the same order of magnitude as the anisotropy effect arising from the different scan strategies (blue vs. green lines). A slightly decreasing tendency is further observed for the width deviation with increasing height. This effect of roughly 0.1 mm is attributed to the decreasing wall thickness. Due to the large scatter and the small distortion of the Wedge sample, this geometry is not suitable as a calibration sample that would allow to better capture wall thickness variations. Nevertheless, it can be used for the validation of the process simulation approaches.

Figure 8 shows similar characteristics and order of magnitudes as observed in previous studies on Inconel 625 [42]. Width deviations are measured as changes of width in the *x*- and *y*-directions in the middle of the sample side faces for the inner and outer contours. While the deformations in the Cross Wall and Wedge geometries are mainly a result of shrinkage in the x/y plane, the characteristic deformation of the Canonical Square sample is a result of the different thermal expansion of the thinner inner and thicker outer structure of the sample. As thermal conduction is limited in the thinner inner section this experiences larger thermal strains than the thicker outer section. When both structures are welded together, the inner section cools off quicker so that compressive stresses are introduced. In this way, the residual deformation in the Canonical Square sample is more dominated by thermal strains in the *z*-direction than by lateral thermal strains in the x/y plane, constituting a different deformation mechanism than the previously presented sample geometries. The resulting structure features a distinct kink in the width deviation of 0.5 mm at the outer contour at a height of 20 mm. A second peak in the width deviation is found at a height of 7.5 mm that is in the order of 0.3 mm. The inner contour on the other hand cannot be characterized completely by 3D laser scanning due to limited accessibility. Width deviations are significantly smaller, however. Anisotropy effects (solid vs. dashed lines) are in the order of 0.02 mm and remain relatively small for the sample printed with a 67° rotating scan strategy.

In summary, a general significant influence of the sample position of up to 0.1 mm and of the scan strategy induced anisotropy in the range of 0.1–0.2 mm is observed. The effect of the sample thickness on the width deviation is in the order of 0.05–0.1 mm. Finally, smaller scale fluctuations on top the global width deviation characteristics are in a range of

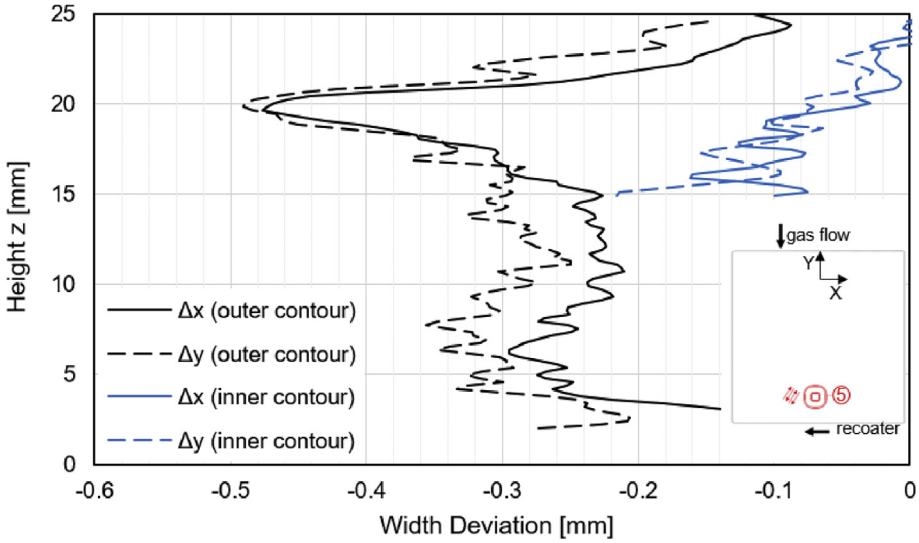

Figure 8. Canonical Square: Measured width deviations in *x*- and *y*-directions (inner and outer contours) for rotating scan strategy.

±0.02 to ±0.05 mm. This is attributed to the surface roughness of the samples with partially molten metal powder particles on the surface which is consistent with reported roughness values of 5μm ≤ Ra ≤ 40 μm for Ti–6Al–4V manufactured by SLM [1, 14].

3.2. Calibration of AAP

The width deviations predicted by the calibrated AAP simulations are compared to the measured distortions in Figure 9. The calibration of *SSF*, $ASC_{\parallel}$ and $ASC_{\perp}$ was performed using CW10 samples with contour scan as printed together with multiple other samples, cf. Section 2.1. Anisotropic strain coefficients ASC_z in *z*-direction were fixed at 1, as recommended by ANSYS. The width deviations of the simulated and measured calibration geometry CW10 were evaluated in the middle of the side walls at a height of $z = 22$ mm and averaged for the *x*- and *y*-directions. The two values were compared and the scaling factors iteratively adjusted to minimize the error to ≤50 μm within the measurement uncertainty level of the 3D laser scanning measurement. For the simulation, AAP prescribes a voxel size of 0.25 mm. Pre-iterations were, however, made with a voxel size of 0.4 mm to obtain a first improved initial value for the subsequent much more numerically expensive optimization with 0.25 mm.

Table 3 lists the relevant calibrated scaling factors for the different simulation types (considering plastic behavior) of AAP. The minor deviation of the ASC values from unity reflects the small anisotropic effect observed in the measured width deviations. Figure 9 compares the predictions of the three calibrated AAP simulation types with the measured width deviations for the 0°/180° bidirectional (top) and the 67° rotating (bottom) CW10 samples. The *ASC* parameters are fitted to the width deviations of the bidirectionally printed sample, while the *SSF* is fitted to the sample printed with rotating scan strategy. The lightly shaded areas indicate the expected error band of the 3D laser scanning method.

As the AS approach does not account for anisotropic effects, the predicted width deviations are equal in *x*- and *y*-directions. While lying well within the error band above 20 mm, the predictions deviate more substantially from the asymmetric width deviations in the lower half of the samples. Consideration of the anisotropic effects within the SP approach improves the prediction for both the bidirectional and rotating

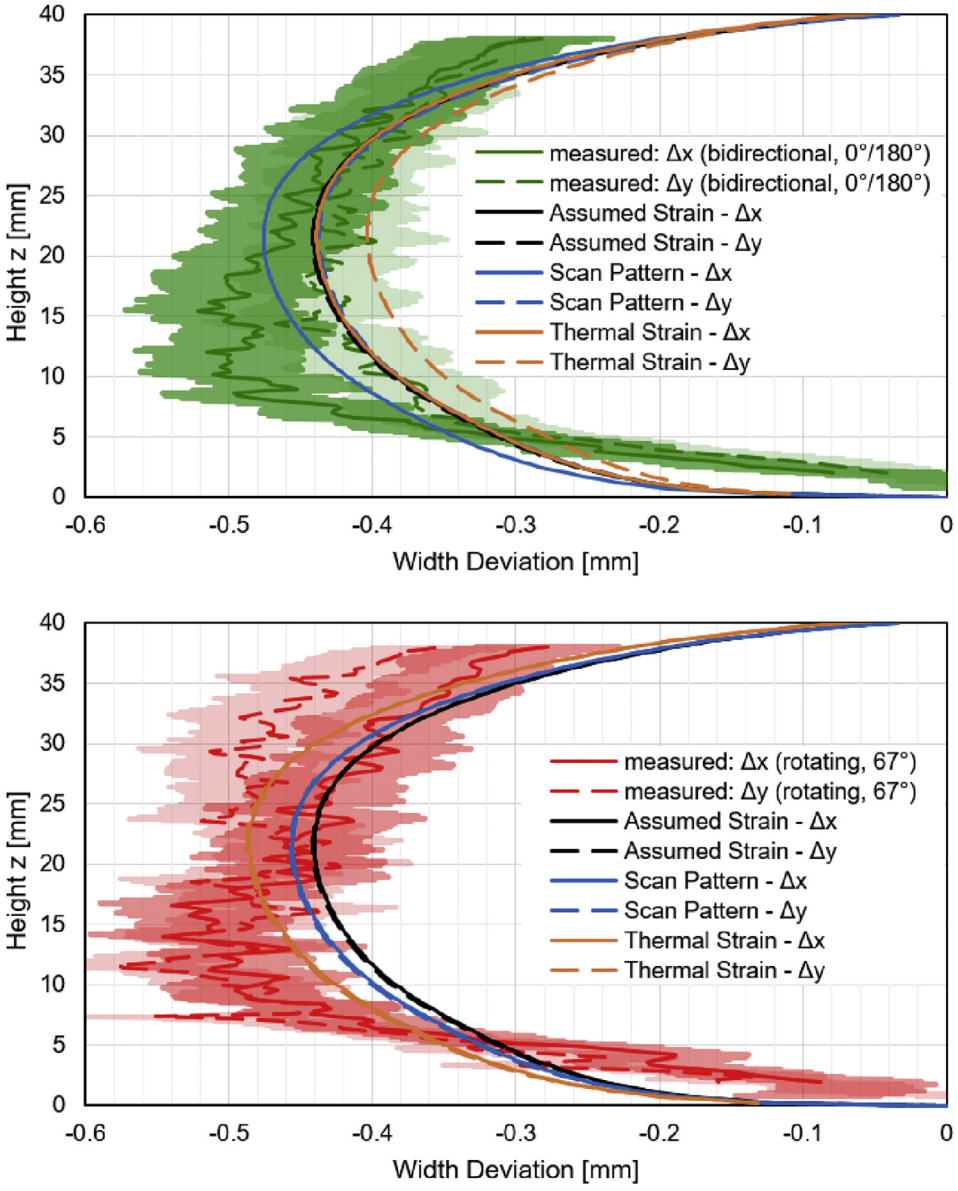

Figure 9. Comparison of measured width deviations (in *x*- and *y*-directions) for bidirectional (top) and rotating (bottom) scan strategies with simulated characteristics after calibration of AAP for the Assumed Strain (black), Scan Pattern (blue) and Thermal Strain (orange) approaches. Error band for as-measured curves is ±0.05 mm.

scan strategies. Still some deviations remain in the lower half of the sample. The TS approach further improves the prediction for the rotating scan strategy as the *SSF* is significantly reduced compared to the other strategies. But the accuracy is reduced for the bidirectional case which is a consequence of the reduced *SSF* that appears to lead to better fits for the isotropic case.

While all three approaches (AS, SP and TS) deliver acceptable representations of the measured data after calibration, uncertainties remain in the prediction of the characteristics in the lower half of the sample. This could be a consequence of neglecting the base plate with its compliance and thermal conductivity or even the presence of minor cracks that relieve the internal stresses and thereby residual strains in vicinity of the base plate. From a practical standpoint, it needs to be judged from the actual problem to be assessed which of the three modelling approaches needs to be used.

The voxel size has a significant influence on the accuracy of the results and the computation time for a given geometry. In AAP the voxel size is chosen so that at least four elements can be placed over the minimum feature thickness. The calculation time increases by a factor of 16 for a decrease of the element size by a factor of 2. For the CW10 sample, a voxel size of 0.25 mm is prescribed for the calibration. In order to estimate the magnitude of the error when calculating with larger voxels, a sensitivity study was performed for the deformations that result for a given voxel size in simulations of bidirectionally printed parts, cf. Figure 10.

3.3. Sensitivity analysis with AAS

As observed for AAP, a variability of the predicted shape deviations with the prescribed element size is expected for AAS. In contrast to AAP, however, AAS is not relying on calibrations but requires appropriate material property input only. A sensitivity analysis was performed with respect to element size and type as well as material property variations as described in the following.

Figure 11 shows the sensitivity of the predicted width deviations both in the CW10 and the Wedge samples resulting from variations in the element size from 1.2 mm to 0.4 mm for hexahedral (HEX) and layered tetragonal (L-TET) meshes. While the qualitative characteristic of the width deviation matches relatively well with the measured data, significant quantitative deviations are observed for AAS simulations especially for L-TET meshes and larger element sizes. The L-TET elements result in roughly 0.05 mm to 0.1 mm larger predicted shrinkage than HEX elements of the same size. Figure 12 shows that the experimental standard deviations significantly reduce with element size. While these appear to converge for the Wedge sample, there is no sign of convergence for the CW10 samples. The finding suggests element sizes as small as 0.2 mm to obtain meaningful predictions of the width change in CW10 samples. This is, however, unpractical from a numerical and storage effort point of view.

In addition to the sensitivity of AAS simulations to element size and type, the variability of the predicted width deviations with respect to material property changes was investigated exemplarily for the Wedge sample. Figure 13 shows the relative changes in width deviation upon a $\pm 10\%$ variation of relevant material properties such as coefficient of thermal expansion α_{th}, melting temperature T_S, elastic modulus E, yield stress σ_y, Poisson ratio υ, in-plane and out-of-plane thermal conductivity $\lambda_{x/y}$ and λ_z, respectively, as well as the thermal heat capacity c_{th}. The largest effect on the variability of the width deviation is observed for α_{th} and T_S which appears to be in the same order of magnitude as the material property variation. Elastic modulus and yield stress also appear to play a significant role with variabilities in the resulting shape deviation as high as $\pm$ 4% resulting from material property variations of $\pm 10\%$. The effect of υ, $\lambda_{x/y}$ and λ_z, as well c_{th} are observed to be comparatively small. Nevertheless, this stresses the importance of a reliable, metal powder specific set of material properties for AAS simulations which can be challenging as these need to be determined reliably up to their melting temperature.

3.4. Simulation of residual deformations

This section compares the various simulation approaches for different sample geometries as printed with 67° rotating scan strategy, in order to provide guidance for the capabilities of the individual methods.

3.4.1. Cross Wall (CW10 and CW2.5)

All considered approaches yield qualitatively comparable simulation results for the width deviations, cf. Figure 14. As the AAP methods Assumed Strain (AS) and Thermal Strain (TS) are both calibrated to CW10 samples, the quantitative agreement between simulation and data is better than AAS. Thereby, the TS approach yields more accurate results than AS as discussed in Section 3.2. For the recommended element size of 0.6 mm, AAS predictions with HEX mesh predict approximately 0.2 mm larger width deviations than measured, while the simulation with L-TET mesh is further off by additional 0.05 mm.

As discussed in Section 3.1, the thinner CW2.5 samples feature comparable shape deviations as the CW10 samples for rotating scan strategies with only a minor shift to larger shape deviations. The AAS simulations with HEX elements, predict 0.02 mm larger width deviations for the thinner samples, while the difference is approximately 0.06mm for simulations with an L-TET mesh. Both simulations with AAP appear to be insensitive to the thickness variation. Due to a tendency of larger measured shape deviations in the thinner CW2.5 sample, the gap between simulation and data is slightly increased. As the wall thickness decreases, larger deviations are expected for the AAP simulations, as the surface contour strategy becomes predominant over the volume scan strategy the software is calibrated to.

3.4.2. Cross Wall (CW10 and CW2.5)

The Wedge samples features a continuously changing thickness with increasing height. Thereby, the volume share of contour to volume strategy increases from the base (20 × 20 mm) to the tip (20 × 0.2 mm) of the wedge. For a merely calibrated approach as followed by AAP, such an extrapolation from the calibrated condition is expected to lead to larger errors. Figure 15 (left) shows that both AAP approaches (i.e. AS and TS), while featuring a similar qualitative characteristic as the measured width deviations, differ by as much as 0.1 mm from the actual values. The slope of the roughly linear width deviation is further smaller than the actually observed slope. In contrast, the uncalibrated AAS approach not only leads to qualitatively but also to quantitatively better agreement between simulation and measurement. Especially, also the predicted slope of the width deviation characteristic matches the

Table 3. Calibrated isotropic strain scaling factors (*SSF*) and Anisotropic Strain Coefficients ($ASC_{\parallel}$, $ASC_{\perp}$) for different simulation types of AAP considering $ASC_Z = 1$ and elastic-plastic material behavior. Error refers to relative deviation of simulated to measured maximum width deviation.

Assumed Strain (AS)			Scan Pattern (SP)			Thermal Strain (TS)		
		error			error			error
SSF	0.64	1.97%	*SSF*	0.66	1.4%	*SSF*	0.45	8.1%
			$ASC_{\parallel}$	1.04	1.2%	$ASC_{\parallel}$	1.04	7.4%
			$ASC_{\perp}$	0.96	1.6%	$ASC_{\perp}$	0.96	6.5%

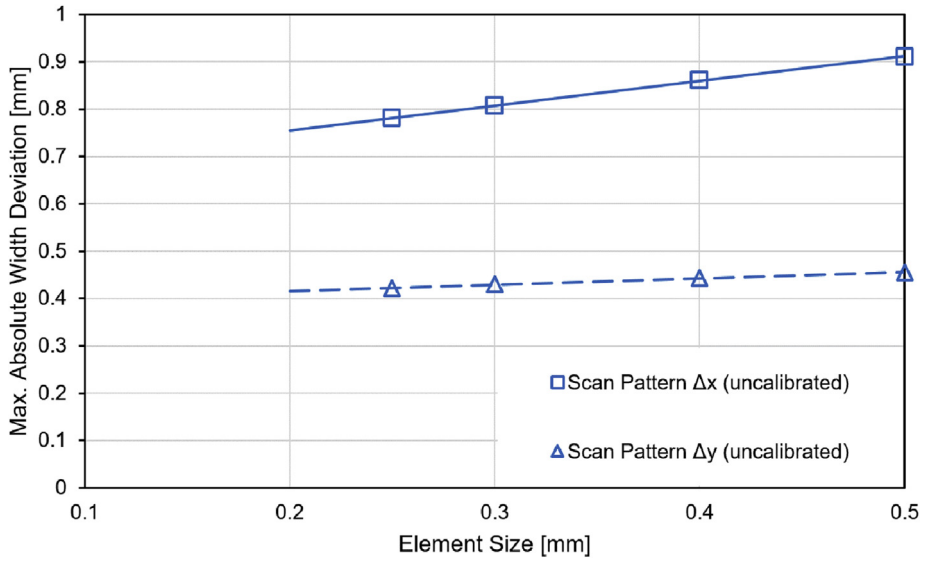

Figure 10. Comparison of width deviations for a bidirectionally brinted CW10 sample for varying voxel element sizes in SP simulations with AAP (uncalibrated simulation).

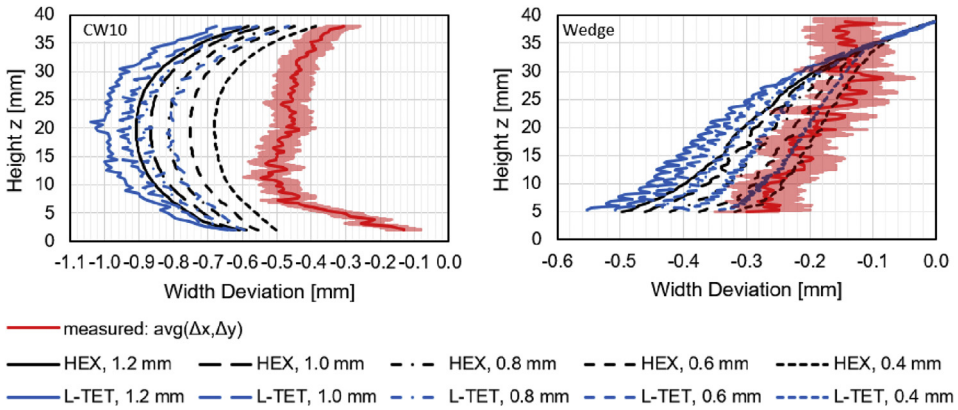

Figure 11. Comparison of measured (red) and simulated width deviations in the CW10 (left) and Wedge (right) samples for varying element size and either hexahedral (HEX, black) or layered tetragonal (L-TET, blue) elements.

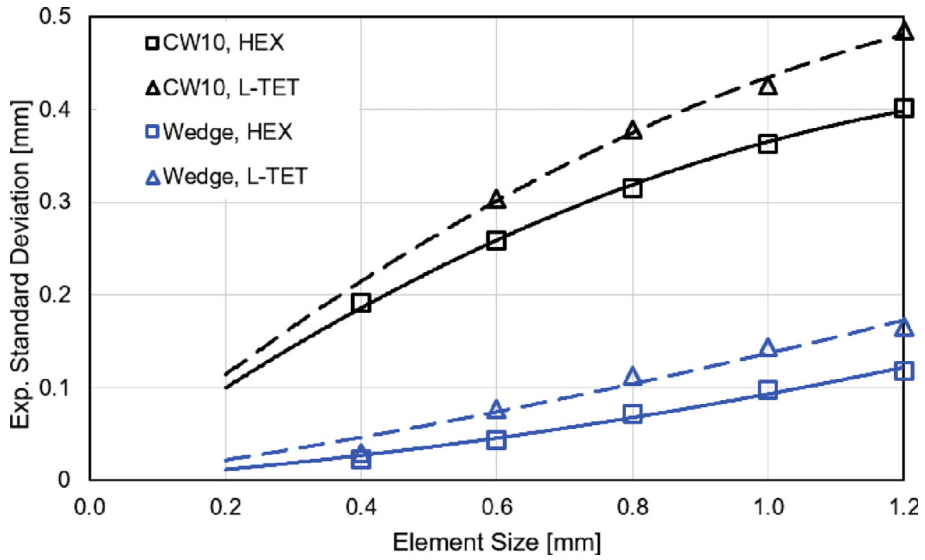

Figure 12. Experimental standard deviations between simulated and measured width deviations in the CW10 (black) and Wedge (blue) samples for hexahedral (HEX, squares) and layered tetrahedral (L-TET, triangles) elements as a function of element size.

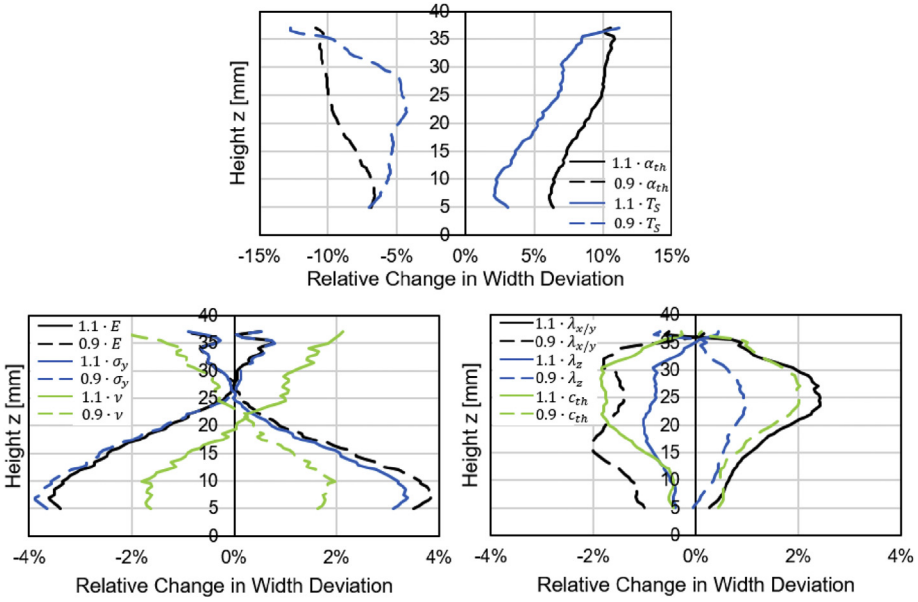

Figure 13. Relative changes of width deviations in the Wedge sample for ±10% variations of relevant input material parameters: α_{th} thermal expansion coefficient, T_S melting temperature, E elastic modulus, ν Poisson ratio, σ_y yield stress, $\lambda_{x/y}$ thermal conductivity in x/y plane, λ_x thermal conductivity in x direction, c_{th} heat capacity.

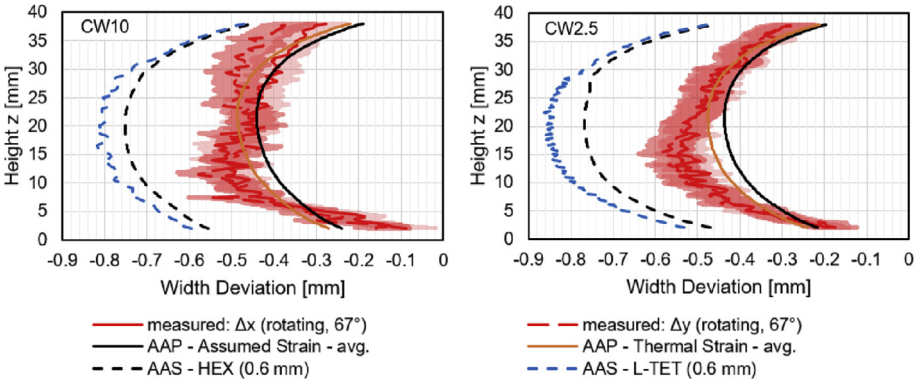

Figure 14. Comparison of width deviations as simulated by AAP (solid lines) and AAS (dashed lines) with measurements for the CW10 (left) and CW2.5 (right) samples printed with rotating scan strategy.

measured data relatively well. As observed also for the CW samples, simulations with L-TET elements lead to larger width deviations than for HEX elements. Furthermore, a change in slope is observed at a height of approximately 32 mm for HEX and 30 mm for L-TET simulations. This is attributed to an insufficient discretization at the tip of the Wedge where less than two elements exist over the thickness of the geometry.

3.4.3. Canonical Square

The Canonical Square geometry constitutes an even more complex geometry for the validation of the simulation approaches. Different wall thicknesses in the inner and outer tubular structures lead to higher average temperatures in the inner section. Due to the larger thermal expansion of the inner tube, a height mismatch develops that leads to a

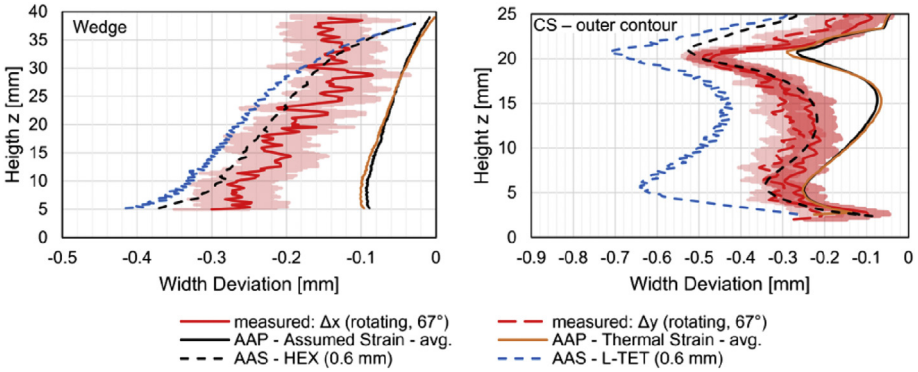

Figure 15. Comparison of width deviations as simulated by AAP (solid lines) and AAS (dashed lines) with measurements for the Wedge (left) and the Canonical Square (right, outer contour only) samples.

significant kink on the outer contour of the Canonical Square when both tubes are merged at a height of roughly 21 mm. Thus, the deformation mechanism is driven less by lateral x/y thermal strains than by vertical thermal expansion in z-direction. As the calibration of the AAP approach in z-direction was neglected, larger deviations in the width deviations are expected for this simulation approach.

Figure 15 (right) compares the width deviation measurements and predictions for the different simulation approaches. Good qualitative agreement is observed for all approaches. Only the AAS simulation with HEX elements, however, also exhibits good quantitative results. For the AAS simulations, the recommended element size of 0.6 mm was used. While a decrease of the element size does not significantly change the peak of the width deviation at $z = 21$ mm, the width deviations significantly decrease in the height range form $z = 5$ mm to 20 mm. As expected, the AAP AS and TS approaches without calibration of the inherent strains in z-direction show significant differences to the width deviation peaks.

4. Conclusions

Simulation of the additive manufacturing process will play an important role in the design of additively manufactured parts and are key to transition from a mere experience based to a more knowledge driven design process that fully exploits the large potential of this manufacturing technique.

This study aimed at presenting a critical insight into the current capabilities of a representative commercially available software package and may serve as benchmark study for future investigations. As software providers are highly engaged into the further development of process simulation software, releasing improvements at a high pace, this study constitutes a snapshot of the current state of development. Besides this, the following conclusions are important for research and industry to get a realistic view on the applicability and reliability of the simulation approaches:

- All presented simulation approaches provide good qualitative predictions of shape deviations in the investigated parts that are within measurement uncertainties of ± 50 µm.
- Calibrated approaches like the inherent strain approach (AAP) are fast and the qualitative results are sufficient to highlight hotspots in a given design; they suffer, however, from a limited extrapolation range from the calibrated geometry.
- More advanced approaches that consider thermal shrinkage of whole layers (AAS) without requiring calibration are comparable in their capability to predict qualitative results. While being highly sensitive to element size and type as well as the material property input, they can provide reasonable qualitative predictions given the necessary care (e.g. element convergence, material data input).
- Qualitative results are sufficient to predict hotspots to improve build orientation, designs and support structures. Quantitative results are required, however, for shape compensation or the prediction of the internal stress state (e.g. for the simulation of heat-treatment effects or mechanical assessments).

Besides the continuous generation of high-quality material data for a wider range of AM alloys that range from room to melting temperature, further development is required to define suitable calibration geometries and strategies, especially to appropriately account for the wide range of support structures and different process parameter sets used in practice. Further research is required to better understand the predictive capabilities of the superlayer approach that is calibrated to any given calibration geometry as well as its limitations that result from the strong simplification of the physical complexity. More appropriate calibration geometries, continuing extension of a more reliable material database, improved user guidelines and increased numerical efficiency are key in the future establishment of the process simulation approaches in the industrial practice.

Declarations

Author contribution statement

Thomas Mayer: Conceived and designed the experiments; Performed the experiments; Analyzed and interpreted the data; Wrote the paper.

Gabriel Brändle & Andreas Schönenberger: Performed the experiments; Analyzed and interpreted the data.

Robert Eberlein: Analyzed and interpreted the data; Contributed reagents, materials, analysis tools or data; Wrote the paper.

Funding statement

This work was funded internally by the ZHAW Institute of Mechanical Systems (IMES). The SLM process was kindly supported by ECOPARTS AG.

Competing interest statement

The authors declare no conflict of interest.

Additional information

No additional information is available for this paper.

References

[1] K. Kempen, et al., Producing crack-free, high density M2 HSS parts by selective laser melting: pre-heating the baseplate, J. Manuf. Sci. Eng. 136 (6) (2013). Dec 2014.
[2] D. Buchbinder, et al., Investigation on reducing distortion by preheating during manufacture of aluminum components using selective laser melting, J. Laser Appl. 26 (2014), 012004.
[3] M.J. Ansari, D.-S. Nguyen, H.S. Park, Investigation of SLM process in terms of temperature distribution and melting pool size: modling and experimental approaches, Materials 12 (2019) 1272.
[4] M. Baumers, et al., Informing Additive Manufacturing technology adoption: total cost and the impact of capacity utilization, Int. J. Prod. Res. (2016), 21 Dec 2016.
[5] P. Bian, X. Shao, J. Du, Finite Element Analysis of thermal stress and thermal deformation in typical part during SLM, Appl. Sci. 9 (2019) 2231.
[6] B. Cheng, K. Chou, Melt pool evolution study in selective laser melting. 26th Annual International Solid Freeform Fabrication Symposium – an Additive Manufacturing Conference, University of Texas, Austin TX, 2015, pp. 1182–1194.
[7] P.S. Cook, A.B. Murphy, Simulation of melt pool behavior during additive manufacturing: underlying physics and progress, Additive Manufacturing 31 (2020) 1–23.
[8] E. Mirkoohi, et al., Heat source modeling in selective laser melting, Materials 12 (13) (2019) 1–18.
[9] M.M. Fyrillas, L. Papadakis, Transient powder melting in SLM using an analytical model with phase change and spherical symmetry in a semi-infinite medium, Journal of Manufacturing and Materials Processing 3 (50) (2019) 1–9.
[10] H. Ali, H. Ghadbeigi, K. Mumtaz, Residual stress development in selective laser-melted Ti6Al4V: a parametric thermal modelling approach, Int. J. Adv. Manufa 97 (2018) 2621–2633.
[11] L. Mugwagwa, et al., Evaluation of the impact of scanning strategies on residual stresses in selective laser melting, Int. J. Adv. Manuf. Technol. 102 (2019) 2441.
[12] L.A. Parry, I.A. Ashcroft, R.D. Wildman, Geometrical effects on residual stress in selective laser melting, Additive Manufacturing 25 (2019) 166–175.
[13] Y. He, et al., Melt pool geometry and microstructure of Ti6Al4V with B additions processed by selective laser melting additive manufacturing, Mater. Des. 183 (2019) 1–13.
[14] J.H. Robinson, et al., The effect of hatch angle rotation on parts manufactured using Selective Laser Melting, Rapid Prototyp. J. 25/2 (2019) 289–298.
[15] C.L.A. Leung, et al., In situ X-ray imaging of defect and molten pool dynamics in laser additive manufacturing, Nat. Commun. 9 (1355) (2018) 1–9.
[16] A.A. Martin, et al., Dynamics of pore formation during laser powder bed fusion additive manufacturing, Nat. Commun. 10 (2019) 1–10, 1987.
[17] P. Stavropoulos, P. Foteinopoulos, Modelling of additive manufacturing processes: a review and classification, Manuf. Rev. 5 (2018) 2.
[18] A.V. Gusarov, et al., Heat transfer modelling and stability analysis of selective laser melting, Appl. Surf. Sci. 254 (4) (2007) 975–979.
[19] L. Hitzler, et al., On the anisotropic mechanical properties of Selective Laser-Melted stainless steel, Materials 10 (1136) (2017) 1–19.
[20] M. Gouge, et al., The Finite Element Methode for the thermo-mechanical modeling of additive manufacturing processes, in: M. Gouge, P. Michaleris (Eds.), Thermo-

Mechanical Modeling of Additive Manufacturing, Butterworth-Heinemann, Oxford UK, 2018.
[21] Y.-X. Wang, et al., Inherent strain method and thermal elastic-plastic analysis of welding deformation of a thin-wall beam, J. Mech. 24 (4) (2008) 301–309.
[22] X. Liang, et al., A modified inherent strain method for fast prediction of residual deformation in Additive Manufacturing of metal parts. 28th Annual International Solid Freeform Fabrication Symposium – an Additive Manufacturing Conference, University of Texas, Austin TX, 2017, pp. 2539–2545.
[23] N. Keller, V. Ploshikhin, New Method for Fast Predictions of Residual Stress and Distortion of AM Parts. 25th Annual International Solid Freeform Fabrication Symposium – an Additive Manufacturing Conference, University of Texas, Austin TX, 2014, pp. 1229–1237.
[24] D. Pal, C. Teng, B. Stucker, Simulation of powder-based additive manufacturing processes, in: T.S. Srivatsan, T.S. Sudarshan (Eds.), Additive Manufacturing – Innovations, Advances, and Applications, CRC Press, Boca Raton, FL, 2016.
[25] H. Bikas, A.K. Lianos, P. Stavropoulos, A design framework for additive manufacturing, Int. J. Adv. Manuf. Technol. 103 (2019) 3769–3783.
[26] L.S. Santos, S.K. Gupta, H.A. Bruck, Simulation of buckling of internal features during selective laser sintering of metals, Additive Manufacturing 23 (2018) 235–245.
[27] T.T. Rühmer, et al., Structural Integrity Assessment and Engine Test of an Additive Manufactured First Stage Ring Segment of a Siemens Large Gas Turbine, in: ASME Turbo Expo 2019, Phoenix AZ, GT2019-90344, 2019, pp. 1–10.
[28] P. Maksimov, et al., Numeric simulation of aircraft engine parts additive manufacturing process, MATEC Web of Conferences (ICMTMTE) 224 (2018) 1–8, 01065.
[29] D. Pal, et al., Simulation of Aerospace Components Fabricated Using Additive Manufacturing, in: 22nd International Symposium on Air Breathing Engines 2015, Phoenix, AZ. ISABE2015-20254, 2015.
[30] K. Terada, T. Miura, N. Kikuchi, Digital image-based modeling applied to the homogenization analysis of composite materials, Comput. Mech. 20 (1997) 331–346.
[31] W.-D. Lian, G. Legrain, P. Cartraud, Image-based computational homogenization and localization: comparison between X-FEM 7 levelset and voxel-based approaches, Comput. Mech. 51 (2013) 1–17.
[32] A. Keβler, Matrix-free voxel-based finite element method for materials with heterogeneous microstructures, Bauhaus-Universität Weimar, PhD Thesis (2017).
[33] ANSYS, Using Additive Print and Additive Science, Release 2019 R1, ANSYS Inc., Canonsburg, PA, 2019.
[34] ANSYS, ANSYS Additive Calibration Guide, Release 2019 R1, ANSYS Inc., Canonsburg, PA, 2019.
[35] ANSYS, ANSYS Workbench Additive Manufacturing Analysis Guide, Release 2019 R1, ANSYS Inc., Canonsburg, PA, 2019.
[36] B. Ferrar, et al., Gas flow effects on selective las melting (SLM) manufacturing performance, J. Mater. Process. Technol. 212 (2012) 355–364.
[37] A.B. Anwar, Q.-C. Pham, Selective laser melting of AlSi10Mg: effects of scan direction, part placement and inert gas flow velocity on tensile strength, J. Mater. Process. Technol. 240 (2017) 388–396.
[38] A.J. Dunbar, et al., Development of experimental method for in situ distortion and temperature measurements during the laser powder bed fusion additive manufacturing process, Additive Manufacturing 12 (2016) 25–30.
[39] America Makes, Developing a Robust Distortion Prediction and Compensation Software Tool – Reduced Product Development Time by 75% - Success story, NCDMM, Blairsville, PA, 2017.
[40] P. Edwards, M. Ramulu, Fatigue performance evaluation of selective laser melted Ti-6Al-4V, Mater. Sci. Eng. 598 (2014) 327–337.
[41] I. Koutiri, E. Pessard, P. Peyre, O. Amlou, T. de Terris, Influence of SLM process parameters on the surface finish, porosity rate and fatigue behavior of as-built Inconel 625 parts, J. Mater. Process. Technol. 255 (2018) 536–546.
[42] J. Irwin, M. Gouge, Validation of the America Makes builds, in: M. Gouge, P. Michaleris (Eds.), Thermo-Mechanical Modeling of Additive Manufacturing, Butterworth-Heinemann, Cambridge, US, 2018.